

ENVIRONMENT OF THE SUBMILLIMETER-BRIGHT MASSIVE STARBURST HFLS3 AT $z \sim 6.34$

N. LAPORTE^{1,2,3}, I. PÉREZ-FOURNON^{1,2}, J. A. CALANOG⁴, A. COORAY^{4,5}, J. L. WARDLOW⁶, J. BOCK^{7,8}, C. BRIDGE⁵,
 D. BURGARELLA⁹, R. S. BUSSMANN¹⁰, A. CABRERA-LAVERS^{1,2,11}, C. M. CASEY⁴, D. L. CLEMENTS¹², A. CONLEY¹³,
 H. DANNERBAUER¹⁴, D. FARRAH¹⁵, H. FU¹⁶, R. GAVAZZI¹⁷, E. A. GONZÁLEZ-SOLARES¹⁸, R. J. IVISON^{19,20}, B. LO FARO⁹, B. MA⁴,
 G. MAGDIS²¹, R. MARQUES-CHAVES^{1,2}, P. MARTÍNEZ-NAVAJAS^{1,2}, S. J. OLIVER²², W. A. OSAGE⁴, D. RIECHERS¹⁰,
 D. RIGOPOULOU^{21,23}, D. SCOTT²⁴, A. STREBLYANSKA^{1,2}, AND J. D. VIEIRA^{5,25}

¹Instituto de Astrofísica de Canarias (IAC), E-38200 La Laguna, Tenerife, Spain

²Departamento de Astrofísica, Universidad de La Laguna (ULL), E-38205 La Laguna, Tenerife, Spain

³Instituto de Astrofísica, Facultad de Física, Pontificia Universidad Católica de Chile, 306, Santiago 22, Chile

⁴Department of Physics & Astronomy, University of California, Irvine, CA 92697, USA

⁵California Institute of Technology, 1200 E. California Blvd., Pasadena, CA 91125, USA

⁶Dark Cosmology Centre, Niels Bohr Institute, University of Copenhagen, Juliane Maries Vej 30, DK-2100 Copenhagen, Denmark

⁷California Institute of Technology, 1200 E. California Blvd., Pasadena, CA 91125, USA

⁸Jet Propulsion Laboratory, 4800 Oak Grove Dr., Pasadena, CA 91109, USA

⁹Laboratoire d'Astrophysique de Marseille, Aix-Marseille University, CNRS, F-13013 Marseille, France

¹⁰Department of Astronomy, Space Science Building, Cornell University, Ithaca, NY 14853-6801, USA

¹¹GTC Project, E-38205 La Laguna, Tenerife, Spain

¹²Astrophysics Group, Imperial College London, Blackett Laboratory, Prince Consort Rd., London SW7 2AZ, UK

¹³Department of Astrophysical and Planetary Sciences, CASA 389-UCB, University of Colorado, Boulder, CO 80309, USA

¹⁴Institut für Astronomie, Universität Wien, Turkenschanzstrasse 17, A-1160 Wien, Austria

¹⁵Department of Physics, Virginia Tech, Blacksburg, VA 24061, USA

¹⁶Department of Physics & Astronomy, University of Iowa, Iowa City, IA 52242, USA

¹⁷Institut d'Astrophysique de Paris, UMR 7095, CNRS, UPMC, Univ. Paris 06, 98bis Blvd., Arago, F-75014 Paris, France

¹⁸Institute of Astronomy, Cambridge University, Madingley Road, Cambridge CB3 0HA, UK

¹⁹European Southern Observatory, Karl Schwarzschild Strasse 2, D-85748 Garching, Germany

²⁰Institute for Astronomy, University of Edinburgh, Royal Observatory, Blackford Hill, Edinburgh EH9 3HJ, UK

²¹Department of Astrophysics, Denys Wilkinson Building, University of Oxford, Keble Road, Oxford OX1 3RH, UK

²²Astronomy Centre, Department of Physics & Astronomy, University of Sussex, Brighton BN1 9QH, UK

²³RAL Space, Science, and Technology Facilities Council, Rutherford Appleton Laboratory, Didcot OX11 0QX, UK

²⁴Department of Physics & Astronomy, University of British Columbia, 6224 Agricultural Road, Vancouver, BC V6T 1Z1, Canada

²⁵Department of Astronomy and Department of Physics, University of Illinois, 1002 West Green St., Urbana, IL 61801, USA

Received 2015 April 17; accepted 2015 July 24; published 2015 September 8

ABSTRACT

We describe the search for Lyman break galaxies (LBGs) near the submillimeter-bright starburst galaxy HFLS3 at $z = 6.34$ and a study on the environment of this massive galaxy during the end of reionization. We performed two independent selections of LBGs on images obtained with the Gran Telescopio Canarias (GTC) and the *Hubble Space Telescope* (*HST*) by combining nondetections in bands blueward of the Lyman break and color selection. A total of 10 objects fulfilling the LBG selection criteria at $z > 5.5$ were selected over the 4.54 and 55.5 arcmin² covered by our *HST* and GTC images, respectively. The photometric redshift, UV luminosity, and star formation rate of these sources were estimated with models of their spectral energy distribution. These $z \sim 6$ candidates have physical properties and number densities in agreement with previous results. The UV luminosity function at $z \sim 6$ and a Voronoi tessellation analysis of this field show no strong evidence for an overdensity of relatively bright objects ($m_{F105W} < 25.9$) associated with HFLS3. However, the overdensity parameter deduced from this field and the surface density of objects cannot exclude definitively the LBG overdensity hypothesis. Moreover, we identified three faint objects at less than 3'' from HFLS3 with color consistent with those expected for $z \sim 6$ galaxies. Deeper data are needed to confirm their redshifts and to study their association with HFLS3 and the galaxy merger that may be responsible for the massive starburst.

Key words: galaxies: formation – galaxies: high-redshift – galaxies: luminosity function, mass function – galaxies: starburst

1. INTRODUCTION

One of the most important questions of modern astronomy is undoubtedly the formation and evolution of the first luminous objects in our universe. Over the past decade, the arrival of new facilities with capabilities to push even further the boundaries of our universe, such as the *Herschel Space Observatory* (Pilbratt et al. 2010), WFC3 on the *Hubble Space Telescope* (*HST*; Robertson et al. 2002), and HAWK-I on the Very Large Telescope (VLT; Pirard et al. 2004), has contributed to considerable advances in our understanding of the first billion years. The number of $z > 6$ galaxies currently confirmed by spectroscopy

has greatly increased over the past few years (e.g., Vanzella 2011; Schenker et al. 2012), allowing us to better constrain their physical properties in terms of the star formation rate (SFR), stellar mass, and reddening (e.g., de Barros et al. 2014). The evolution of such galaxies is now relatively well constrained and supported by spectroscopic observations out to $z \sim 6$ (e.g., LeFevre et al. 2015), and photometric studies are now slowly starting to give robust constraints of galaxies out to $z \sim 10$ (e.g., Bouwens et al. 2014).

The detection of large numbers of dusty, massive starburst galaxies at $z \sim 2$ was a surprise when they were first identified

Table 1
Photometric Properties of the Imaging Data

Filter	λ_{eff} (nm)	$\Delta\lambda$ (nm)	t_{exp} (ks)	$m(5\sigma)$	Instrument
(1)	(2)	(3)	(4)	(5)	(6)
g'	481.5	153	2.7	26.91 ^a	OSIRIS/GTC
r'	641.0	176	2.7	26.80 ^a	OSIRIS/GTC
i'	770.5	151	21.6	26.60 ^a	OSIRIS/GTC
z'	969.5	261	16.3	25.87 ^a	OSIRIS/GTC
F625W	629.6	98	1.6	26.08 ^b	ACS/ <i>HST</i>
F814W	811.5	166	2.3	26.99 ^b	ACS/ <i>HST</i>
F105W	1055.1	265	9.9	25.90 ^c	WFC3/ <i>HST</i>
F125W	1248.6	443	4.4	26.30 ^c	WFC3/ <i>HST</i>
F160W	1536.9	268	2.8	26.00 ^c	WFC3/ <i>HST</i>
K_s	2150.0	320	3.6	23.14 ^a	LIRIS/WHT
3.6 μm	3575.0	776	3.8	24.38 ^d	IRAC/ <i>Spitzer</i>
4.5 μm	4528.0	1060	3.8	24.30 ^d	IRAC/ <i>Spitzer</i>

Notes. (1) Filter identification, (2) filter central wavelength, (3) filter width, (4) exposure time, (5) 5σ AB magnitude, and (6) instrument and telescope.

^a Point-source depth measured in a $1''.4$ radius aperture.

^b Point-source depth measured in a $0''.25$ radius aperture.

^c Point-source depth measured in a $0''.50$ radius aperture.

^d Point-source aperture-corrected depth measured in a $1''.9$ radius aperture.

in 1997 (Smail et al. 1997; Hughes et al. 1998; for a review see Casey et al. 2014). Theoretically, the existence of dusty starbursts at such early epochs is difficult to explain, and thorough observational constraints on their properties provide a stringent test of the galaxy formation models (e.g., Baugh et al. 2005). The *HerMES* survey (Oliver et al. 2012) has identified a population of dusty starburst galaxies at $z \geq 4$ (Dowell et al. 2014) that are not predicted by today's galaxy formation paradigms (e.g., Hayward et al. 2012). The efficient identification and detailed study of these rare $z \geq 4$ starbursting galaxies are important for understanding their progenitor populations, drivers of cold gas accretion (Carilli et al. 2010), and their descendants. It has been shown by previous studies that several massive starbursts at high z could be protocluster members, but none of them have been identified at $z \geq 6$ (Daddi et al. 2009; Capak et al. 2011).

Recently, Riechers et al. (2013) have discovered an extreme submillimeter starburst at $z = 6.34$, called HFLS3 hereafter, over 21 deg^2 of the *Herschel*/SPIRE (Griffin et al. 2010) data from the *HerMES* survey. This object is lensed by a two-component galaxy system at $z \sim 2.1$ involving a magnification of 2.2 ± 0.3 (Cooray et al. 2014). Its physical properties based on the rest-frame UV emission result in an SFR of $1320 M_{\odot} \text{ yr}^{-1}$ and dust and stellar masses of $3 \times 10^8 M_{\odot}$ and $5 \times 10^{10} M_{\odot}$, respectively, making this source one of the most massive starbursts currently known during the epoch of reionization (EoR).

A recent paper aiming to detect submillimeter emission in the vicinity of HFLS3 with SCUBA-2 data (Robson et al. 2014) found no evidence in favor of an overdensity of dusty galaxies associated with HFLS3. In this paper, we present results of an optical and near-IR (NIR) analysis of the environment of HFLS3, aiming to recover Lyman break galaxies (LBGs) at $z \sim 6$. We combine two data sets:

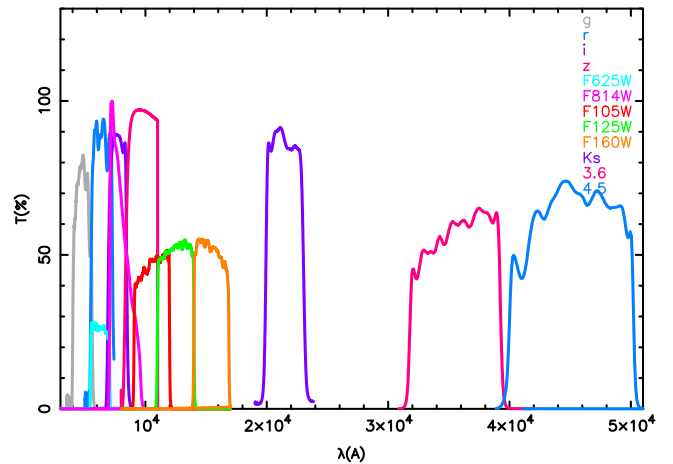


Figure 1. Wavelength coverage and filter transmission.

ground-based images covering a wide field of view (to select the brightest objects at $z \sim 6$), and deeper *HST*/WFC3 and ACS data with a smaller field of view (to detect fainter objects).

In Section 2, we present our new data used for the analysis and their reduction procedure. In Section 3, we explain in detail the method that was used to select $z \sim 6$ objects and present the candidates coming from the two ground- and space-based data sets. Their photometric properties are presented in Section 4. In Section 5 we discuss the presence of an overdensity of LBGs in the HFLS3 field. The concordance cosmology is adopted throughout this paper, with $\Omega_{\Lambda} = 0.7$, $\Omega_m = 0.3$, and $H_0 = 70 \text{ km s}^{-1} \text{ Mpc}^{-1}$. All magnitudes are quoted in the AB system (Oke & Gunn 1983).

2. OBSERVATIONS AND DATA REDUCTION

In this section, we present the ground-based and space-based data we used to perform the search for $z \sim 6$ objects around HFLS3. GTC optical and *Spitzer* data have already been presented in Riechers et al. (2013). We have re-reduced the GTC data to improve their image qualities, and we include a newly acquired K_s -band image taken with LIRIS on the the 4.2 m William Herschel Telescope (WHT). In the following we summarize image properties and the data reduction procedure. A summary of the data used in the current study is listed in Table 1, and Figure 1 shows the wavelength coverage of our study.

2.1. Ground-based Data

In order to select bright objects at $z \sim 6$ and to establish the bright end of the UV luminosity function (LF; Lacey et al. 2011), we performed a first search for LBGs in ground-based images taken with OSIRIS on GTC (Alvarez et al. 1998; Cepa et al. 2003) and LIRIS installed on WHT (Wall 1987; Manchado et al. 1998).

OSIRIS data were acquired between 2011 June 29 and August 3, as part of the GTC2-10ITP program (P.I.: I. Pérez-Fournon), and used g' , r' , i' , and z' broadband filters. The field of view covered by OSIRIS is $7'.8 \times 7'.8$, and the total exposure times in each band are 2.7 ks in g' and r' , 21.6 ks in i' , and 18.7 ks in z' . Each frame was reduced individually following the standard reduction procedure in IRAF²⁶ (bias

²⁶ <http://iraf.noao.edu/>

subtraction, flat-fielding, sky subtraction) and registration and combination using SCAMP (Bertin 2006) and SWARP (Bertin 2010). To reduce the sky background at long wavelengths, we applied for the i' - and z' -band images a double sky subtraction using the IRAF package XDIMSUM, with steps explained in Richard et al. (2006). The astrometric and photometric calibrations were performed using the 9th release of the SDSS catalog (Ahn et al. 2012). Moreover, to produce the best z -band quality image, we applied the “best seeing stacks” method described in Gwyn (2012), selecting only the best frames in terms of seeing. We measured the FWHM on each frame using PSFEx (Bertin 2011), and we kept 86.4% of our original data set beyond which the FWHM increases without a significant evolution of the image depth. The seeing of the final images is $0''.89$, $0''.83$, $0''.83$, and $0''.89$ respectively, in g' , r' , i' , and z' . The depth was computed using empty $1''.4$ radius apertures all over the field.

We added to our previous data set a new NIR, K_s image acquired on 2014 June 5 with the LIRIS instrument ($4'.27 \times 4'.27$ field of view, $0''.25$ size pixels) installed at the Cassegrain focus of the WHT, as part of a new WHT Large Program on HerMES high-redshift galaxies (P.I.: I. Pérez-Fourmon). The total integration time was 3.6 ks, the observing conditions were photometric, and the seeing was $0''.5$. The reduction of the image was performed using the IAC’s IRAF `lirisdr` task,²⁷ and the astrometry calibration was carried out using the Graphical Astronomy and Image Analysis Tool (GAIA) included in the Starlink astronomical software package.^{28,29} The K_s image was matched to SDSS DR10 stars and is estimated to be accurate to $0''.1$ (rms of the fit). The photometric calibration of the image was done with Two Micron All Sky Survey stars. The 5σ depth of this image in $1''.4$ radius apertures is 23.14.

2.2. Space-based Data

The data reduction of the ACS and WFC3 data we used in this study is described in detail in Cooray et al. (2014). We summarize hereafter the principal steps. These data are part of an *HST* Cycle 21 program (GO 13405, PI: A. Cooray) and used six orbits to produce images of the HFLS3 environment in F625W, F814W, F105W, F125W, and F160W (Table 1). We used the IRAF.STSDAS pipeline and the CALWFC3 tool for flat-fielding and cosmic-ray rejections and ASTRODRIZZLE (Fruchter et al. 2010) to combine individual exposures and create $0''.06 \text{ pixel}^{-1}$ WFC3 images. The ACS data were flat-fielded, charge transfer efficiency corrected, and cosmic rays rejected using the CALACS pipeline (version 2012.2), and then combined with ASTRODRIZZLE to produce $0''.03 \text{ pixel}^{-1}$ images. Astrometric calibration was performed using SDSS (9th release). The WFC3 and ACS data were matched independently following the classical IRAF procedure. The depth was computed using empty apertures all over the field ($0''.25$ radius for ACS and $0''.50$ radius for WFC3 images).

In order to extend the wavelength coverage of our survey, we also used data obtained with IRAC (Fazio et al. 2004) on board the *Spitzer Space Telescope* as part of a DDT program (ID: 80240—PI: J. Vieira) on 2012 March 21. The on-target

observations consisted of 38 frames with an integration time of 100 s in each of the two channels centered at $3.6 \mu\text{m}$ (ch1) and $4.5 \mu\text{m}$ (ch2). We used corrected basic calibrated data (cBCD) frames, which are already corrected by pipeline for various artifacts, such as multiplexer bleed and pulldown. These images, together with associated mask and uncertainty images, were processed, drizzled (with a PIXFRAC of 0.65), and combined using the standard pipeline MOPEX. The final mosaic images have a pixel size of $0''.6$, roughly half of the IRAC native pixel scale. The mosaic has a 3σ point-source sensitivity of 0.384 and $0.412 \mu\text{Jy}$ in 3.6 and $4.5 \mu\text{m}$, respectively.

2.3. Source Catalogs

We used SExtractor 2.18.4 (Bertin & Arnouts 1996) to build catalogs in double-image mode using a χ^2 image including all individual pictures, as the detection picture (Szalay et al. 89). The extraction parameters we used have been chosen in order to extract faint objects. Therefore, the DETECT_MINAREA parameter was fixed to 4.0 pixels according to the seeing of our images, and to limit spurious detections, we choose DETECT_THRESH = 1.7σ (e.g., see Muzzin et al. 2013), DEBLEND_NTHRESH = 16, and DEBLEND_MINCONT = 0.00002 (Scoville et al. 2007). We measured the photometry in apertures with radius defined by $2 \times \text{FWHM}$ on point-spread function (PSF) matched data on the GTC data and $0''.4$ radius aperture on *HST* images, as well as with SExtractor MAG_AUTO. We found that these two types of magnitude are in good agreement for all point-source-like objects in our catalogs.

3. SELECTION OF $z \sim 6$ LYMAN BREAK GALAXIES

The LBG technique (Steidel et al. 1996) has been extensively used to select galaxies at high z (e.g., Castellano et al. 2010; Trenti et al. 2012; Laporte et al. 2014). It combines two different criteria: nondetection/detection and the color selection. We applied this method on SExtractor catalogs (Bertin & Arnouts 1996) built using detection parameters as a function of the data set we used (see below for details). Regarding the depth and spatial resolution of each data set, we performed independent searches in each survey: from our ground-based images we focused on the brightest objects, and from the *HST* data we investigated faintest sources at the redshift of HFLS3.

3.1. Selection from GTC Data

The GTC/OSIRIS imaging data we used to search for LBGs at the redshift of HFLS3 covered a wavelength range between 328.5 and 1230.5 nm. The nondetection/detection criteria we applied to our catalogs to select $z \sim 6$ objects were the following:

$$m_{g'} > m(2\sigma)_{g'} = 27.9 \quad (1)$$

$$m_{r'} > m(2\sigma)_{r'} = 27.8 \quad (2)$$

$$m_{z'} < m(5\sigma)_{z'} = 25.9. \quad (3)$$

The lack of deep NIR data over the OSIRIS field of view does not allow us to produce a color–color diagram with a clear selection window.

We defined a color window using the $i' - z'$ color evolution of a set of templates (Bruzual & Charlot 2003 and Polletta

²⁷ www.iac.es/galeria/jap/lirisdr/LIRIS_DATA_REDUCTION.html

²⁸ <http://star-www.dur.ac.uk/~pdraper/gaia/gaia.html>

²⁹ <http://starlink.jach.hawaii.edu/starlink>

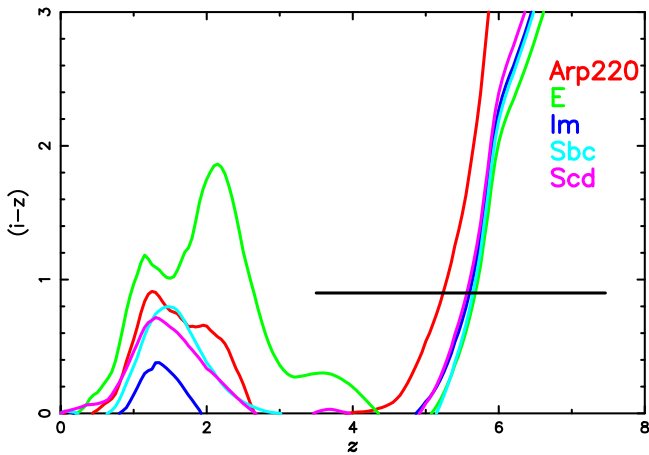


Figure 2. $i' - z'$ color cut defined for the $z \sim 6$ LBG selection using GTC filters and color evolution of several templates of galaxies (Bruzual & Charlot 2003; Polletta et al. 2007). The color criterion is defined by the black line and shows that in that case the majority of the contaminants are elliptical galaxies at mid- z values.

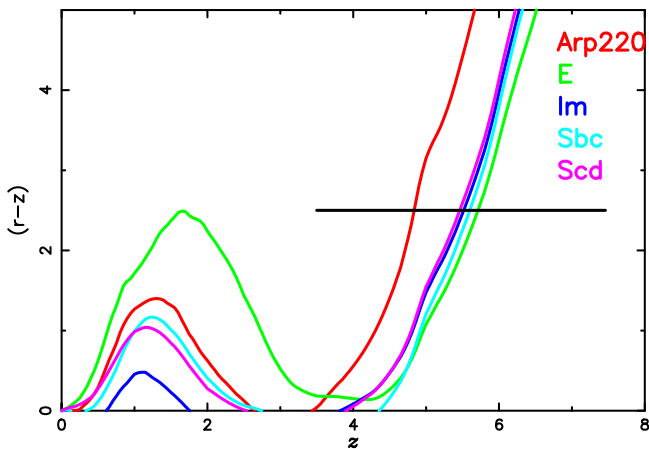


Figure 3. $r' - z'$ color window defined for the $z \sim 6$ LBG selection using GTC filters.

et al. 2007) as a function of the redshift (Figure 2; $m_i - m_z > 0.9$). These criteria limit the contamination by most of the low- z interlopers, except for the elliptical galaxies at $z < 3$. In order to avoid the contamination by such interlopers, we estimated the size of the break between optical and NIR, beyond which the selection of mid- z interlopers is unlikely (Figure 3). The break required by the evolution of templates mentioned above ($m_r - m_z > 2.5$ mag) is consistent with the nondetection criteria that we applied, and thus by combining the previous $i' - z'$ color criterion ($m_i - m_z > 0.9$ mag) with the nondetection/detection criteria listed above, we eliminate a large number of mid- z interlopers. Therefore, we can summarize the color selection we defined to select $z \sim 6$ objects on the GTC data as follows:

$$m_i - m_z > 0.9$$

$$m_r - m_z > 2.5.$$

The selection window is shown in Figure 4.

After visual inspection, only two objects satisfy the selection criteria defined above with $m_z < 25.1$. These two candidates are displayed as z1_GTC and z2_GTC in Figure 5 and Table 2.

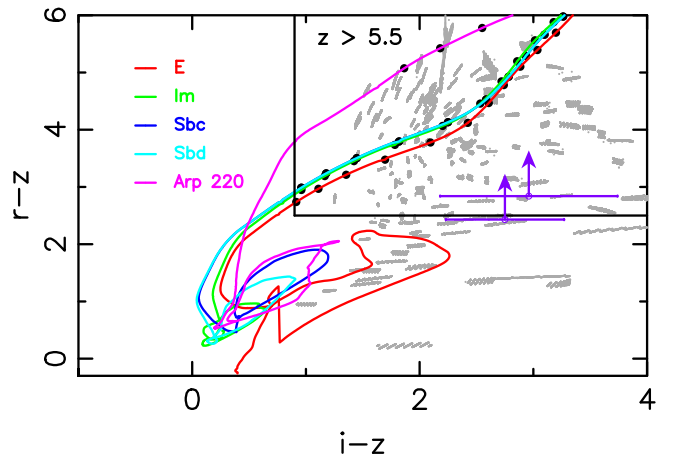


Figure 4. Color criteria used to select $z > 5.5$ objects using templates from Bruzual & Charlot (2003) and Polletta et al. (2007). Positions of the two GTC candidates are displayed by magenta dots. We overlotted the expected color of M, L, and T dwarfs in gray computed from 225 stellar spectra (see references in Section 3.4). Black dots show the colors of objects with redshift ranging from 5.5 to 6.5 per bin of 0.1.

3.2. Selection from HST Data

The second sample has been built using *HST* data covering wavelength from 580.6 to 1670.9 nm. In order to select $z \sim 6$ objects, and regarding the set of filters we have, we defined the following detection/nondetection criteria:

$$m_{F625W} > m(2\sigma)_{F625W} \cup m_{F105W} < m(5\sigma)_{F105W} \quad (4)$$

or in terms of color,

$$m_{F625W} - m_{F105W} > 1.2. \quad (5)$$

The wavelength coverage of the *HST* data is better in the NIR domain compared to the GTC survey. Therefore, we can define a color window to select $z \sim 6$ objects following the standard method described in Section 3.1. Figure 6 displays this selection window, defined by

$$m_{F625W} - m_{F814W} > 2.0 \quad (6)$$

$$m_{F814W} - m_{F105W} < 4.0 \quad (7)$$

$$m_{F625W} - m_{F814W} > 0.57 \times (m_{F814W} - m_{F105W}) + 0.66. \quad (8)$$

The use of broadband filters, as well as color selection, implies that several of the $z \sim 6$ candidates will be lost during the selection process. In order to estimate the fraction of those objects, we computed the incompleteness of the selection function described in this paper. Using templates from Coleman et al. (1980), Kinney et al. (1996), Polletta et al. (2007), and Silva et al. (1998) and transmission of filters used in this survey, we simulated 100,000 objects in the redshift range $4.0 < z < 8.0$ per bin of 0.25 mag with m_{F105W} ranging from 19.0 to 29.0. The selection by the color criteria defined above shows that $\sim 74\%$ of objects at $z \sim 6.3$ are selected.

As previously, we used SExtractor 2.18.4 in double-image mode using a χ^2 image (Szalay et al. 1999) made with the WFC3 images as the detection picture to produce WFC3 catalogs, because $z \sim 6$ LBGs should be detected at these wavelengths. As in the “ground-based” selection, we used SExtractor parameters defined to maximize the selection of faint objects. We then used TOPCAT (Taylor 2005) to match

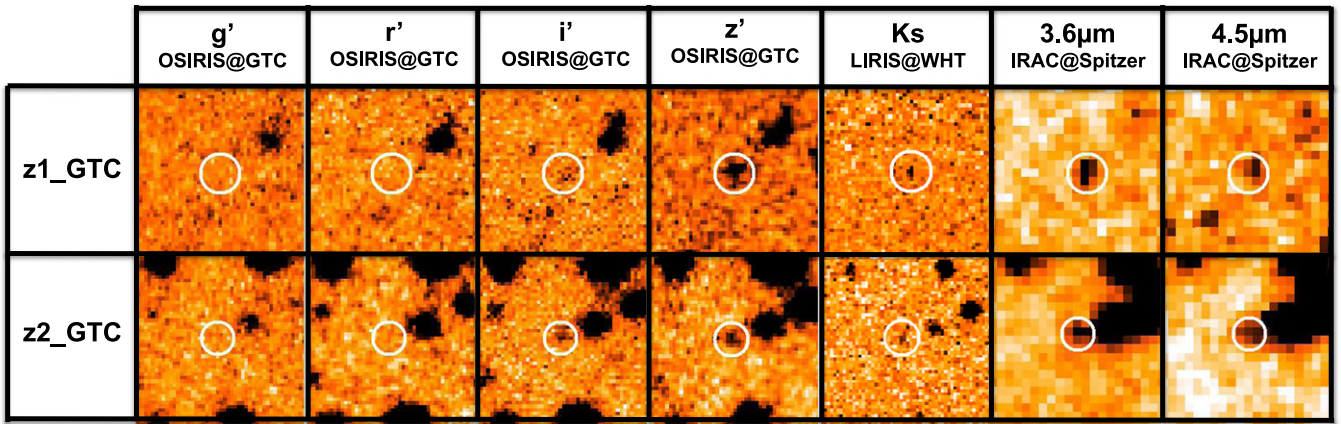


Figure 5. Thumbnail images of the two candidates selected in the $7'8 \times 7'8$ OSIRIS field of view. The size of each stamp is $12'' \times 12''$. The position of the candidate is displayed by a white circle of $1'4$ radius aperture.

Table 2
Photometry of the Two Candidates Selected from the GTC/OSIRIS Data

ID	R.A.	Decl.	m_g	m_r	m_i	m_z	m_{Ks}	$m_{3.6}$	$m_{4.5}$
z1_GTC	17:06:40.6	+58:47:49.6	>27.9	>27.8	27.92	24.96	23.08	23.24	24.73
					± 0.77	± 0.10	± 0.22	± 0.08	± 0.22
z2_GTC	17:06:41.310	+58:47:17.28	>27.9	>27.8	27.48	25.05	23.62	22.91	23.00
					± 0.51	± 0.11	± 0.36	± 0.20	± 0.20

Note. All GTC magnitudes are MAG_AUTO magnitude from SExtractor. Upper limits are 2σ depth. Error bars are computed within empty $1'4$ radius apertures around the object on the GTC data. IRAC magnitudes are measured in a $1'9$ radius aperture, and error bars are computed using an empty $1'9$ radius aperture around the object.

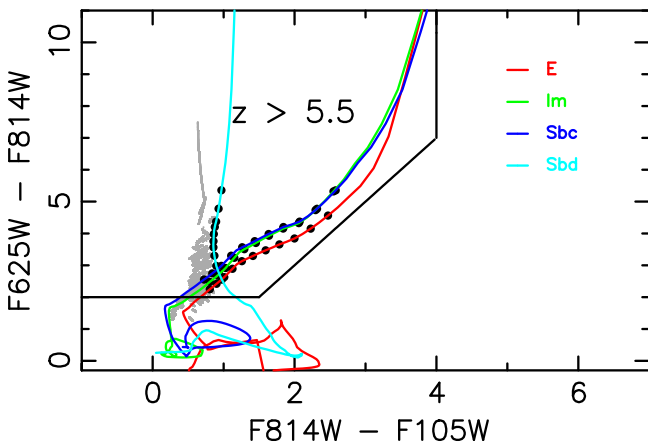


Figure 6. F625W–F814W–F105W color window defined for the $z \sim 6$ LBG selection using *HST* filters and color evolution of several templates of galaxies given by Bruzual & Charlot (2003) and Polletta et al. (2007). The color criteria for $z > 5.5$ are defined by the black box. We overplotted the expected color of M, L, and T dwarfs in gray computed from 225 stellar spectra (see references in Section 3.4). Black dots show the colors of objects with redshift ranging from 5.5 to 6.5 per bin of 0.1.

ACS single-image mode catalogs with the WFC3 catalogs allowing a search radius fixed to $2 \times \text{FWHM}$ of the worst seeing image. The total magnitude was obtained from aperture correction using F160W MAG_AUTO and following the method described in Finkelstein et al. (2013). Each catalog included ~ 1600 detections. Colors were measured on PSF-matched data, and 14 objects follow the criteria defined above. Among these sources, one of our GTC candidates is covered by the *HST* field of view and is included in this new sample (ID: z2_GTC), showing that our two selection functions are well

defined to select this kind of object. The other GTC candidate (z1_GTC) is not detected on the F625W images and well detected on the F814W images ($m_{F814W} = 26.80 \pm 0.18$), confirming the break between the i' and z' band of our GTC survey. However, HFLS3 is not included in this sample, because SExtractor failed to extract it properly; it is blended with the two nearby $z \sim 2.1$ galaxies acting as a foreground lens (see Cooray et al. 2014 for more details). Five objects have been removed from this sample because they are detected on the deep g' -band data from the GTC survey (see Section 3.4 for details). Therefore, the final sample is composed of nine objects and is presented in Table 3 and Figure 7.

3.3. Detection in LIRIS and IRAC Data

We increased the number of spectral energy distribution (SED) constraints in the NIR domain by using data from LIRIS and IRAC. Owing to the depth of our K_s image, only the two GTC objects are clearly detected in the NIR (including the candidate in common in the two samples). These results are not surprising regarding the brightness of these sources, but it could have been a way to remove mid- z interlopers from the *HST* sample. Indeed, previous papers have shown that mid- z interlopers display a very high z LBG like SED up to $1.6 \mu\text{m}$, but they are very red at larger wavelengths corresponding to IRAC (e.g., Boone et al. 2011). The depth of IRAC data ($m_{3.6,4.5} (5\sigma) \sim 24.3$) is not completely sufficient to add robust constraints on the SEDs of all our candidates. Among the two different samples, two objects are clearly detected in the IRAC data. We extracted the photometry of z2_GTC using *imfit*.³⁰ For both objects, we measured the photometry in a $1'9$

³⁰ www.mpe.mpg.de/~erwin/code/imfit/index.html

Table 3
Photometry of the Candidates Selected in the *HST* Data

ID	R.A.	Decl.	m_{F625}	m_{F814}	m_{F105}	m_{F125}	m_{F160}	$m_{3.6}$	$m_{4.5}$
z1_HST	17:06:41.310	+58:47:17.28	>27.08	26.42	24.52	24.09	23.90	22.91	23.00
				± 0.13	± 0.07	± 0.03	± 0.03	± 0.20	± 0.20
z2_HST	17:06:40.737	+58:46:58.52	>27.08	>27.99	25.08	25.37	25.08	>25.38	>25.30
					± 0.11	± 0.10	± 0.09		
z3_HST	17:06:57.157	+58:46:31.85	>27.08	27.01	25.34	25.07	25.09	>25.38	>25.30
				± 0.23	± 0.13	± 0.07	± 0.09		
z4_HST	17:06:40.411	+58:47:01.39	>27.08	27.91	25.81	25.53	25.53	>25.38	>25.30
				± 0.47	± 0.20	± 0.11	± 0.14		
z5_HST	17:06:55.049	+58:46:39.05	>27.08	>27.99	25.87	25.61	25.60	>25.38	>25.30
					± 0.21	± 0.12	± 0.15		
z6_HST	17:06:40.212	+58:45:57.16	>27.08	>27.99	25.92	25.64	25.81	>25.38	>25.30
					± 0.23	± 0.12	± 0.18		
z7_HST	17:06:45.315	+58:46:39.78	>27.08	26.73	25.94	25.67	25.68	>25.38	>25.30
				± 0.15	± 0.23	± 0.13	± 0.16		
z8_HST	17:06:45.289	+58:45:20.86	>27.08	27.67	26.11	25.80	26.01	>25.38	>25.30
				± 0.37	± 0.27	± 0.14	± 0.22		
z9_HST	17:06:49.819	+58:46:58.26	>27.08	26.86	26.47	26.45	26.43	>25.38	>25.30
				± 0.18	± 0.37	± 0.25	± 0.32		

Note. All *HST* magnitudes are MAG_AUTO magnitude from SExtractor. Upper limits are 2σ depth. Error bars are computed within empty $0''.125$ radius apertures around the object on the ACS data and $0''.25$ radius on WFC3 data. IRAC magnitudes are measured in a $1''.9$ radius aperture, and error bars are computed using empty $1''.9$ radius apertures around the object.

radius aperture and used the correction factor computed by Mauduit et al. (2012). The error bar was computed using empty $1''.9$ radius apertures around the object.

3.4. Contaminants

The most common sources of contamination of high- z samples are supernovae (SNe), active galactic nuclei (AGNs), low-mass stars, photometric scatter, transient objects, spurious sources, and extremely red galaxies, among others. All our candidates are detected in at least two bands, limiting the contaminations by spurious sources; moreover, these observations spread over several months, limiting the detection of transient sources. However, we noted that our ample is not free of AGN and SN contamination given the timescale during which our observations have been carried out. Regarding the field of view covered by these two surveys and the statistical number of SNe expected in $\sim 1 \text{ deg}^2$, the probability of being contaminated by an SN is relatively small. Low-mass stars, such as M, L, and T dwarfs, could display the same color properties as those expected for high- z galaxies. We computed the expected colors of these galaxies through all the filters we used in this study from 225 stellar spectra (Cruz et al. 2004; Burgasser et al. 2006a, 2006b, 2006c, 2006d, 2007, 2008; Chiu et al. 2006; McElwain et al. 2006; Reid et al. 2006; Liebert et al. 2007; Looper et al. 2007; Siegler et al. 2007; Sheppard et al. 2009; Kirkpatrick et al. 2010). Figures 6 and 4 display the expected colors of these stars that are consistent with previous studies (e.g., Willott et al. 2013; Finkelstein et al. 2014) and show that stellar contamination is non-negligible in both samples. Therefore, to limit the selection of low-mass stars, expected to be unresolved on our data set, we used SExtractor FLUX_RADIUS enclosing 50% of the total flux and the SExtractor stellarity parameter. Both indicators demonstrate that two objects among our samples are likely unresolved, namely, z1_HST and z3_HST with a stellarity parameter of >0.7 and a size computed from the half-

light radius comparable with the FWHM of the image, taking uncertainties into account.

Therefore, the majority of contaminants that can enter into our sample involve the extremely red mid- z galaxies. We estimated the contamination rate of our sample by mid- z interlopers by using the color distribution of mid- z objects over the fields of view covered by our two data sets (e.g., Oesch et al. 2010). We followed a three-step method summarized hereafter: (1) we selected all objects that are detected at more than 2σ in all bands, (2) then we matched the luminosity range to the luminosity covered by our two samples and added the corresponding uncertainties on the photometry, and (3) finally we applied the selection criteria we used to build our high- z candidate samples, and all the selected objects are mid- z interlopers. Three objects are identified over the 4.5 arcmin^2 covered by *HST* data, and two using our GTC data, leading to $\sim 7\%$ – 36% and $>20\%$ contamination rate including cosmic variance, respectively. It has been shown by several recent studies (e.g., Hayes et al. 2012; Laporte et al. 2015) that the best way to remove such objects is to cover the short wavelength with deeper imaging data, regarding that the contamination rate by such extreme mid- z interlopers is rather uncertain. We used our deep GTC g' -band data to confirm the real nondetection of *HST* candidates. We find that one of our targets is clearly detected ($m_g \sim 4\sigma$) and cannot, therefore, be at $z \sim 6$. Four other candidates are faint in that image ($m_{g'} \sim 2\sigma$) and thus cannot also be at such high z , but further data are necessary to confirm their optical emission.

After removing these mid- z interlopers, the final *HST* sample is composed of nine objects, with m_{F105} ranging from 24.5 to 26.5 (Figure 8). The postage stamps are displayed on Figure 7, and Table 3 presents the photometry of this sample.

We note here that our ACS images are not deep enough to exclude definitively the low- z hypothesis for all our $z \sim 6$ galaxy candidates. Indeed, the 2σ depth of the F625W image used here (27.1 AB), combined with the F814W depth (27.99 AB), does not allow us to apply completely the color-color criteria we imposed (F625W–F814W > 2.0). For most of them, the F625W–F814W

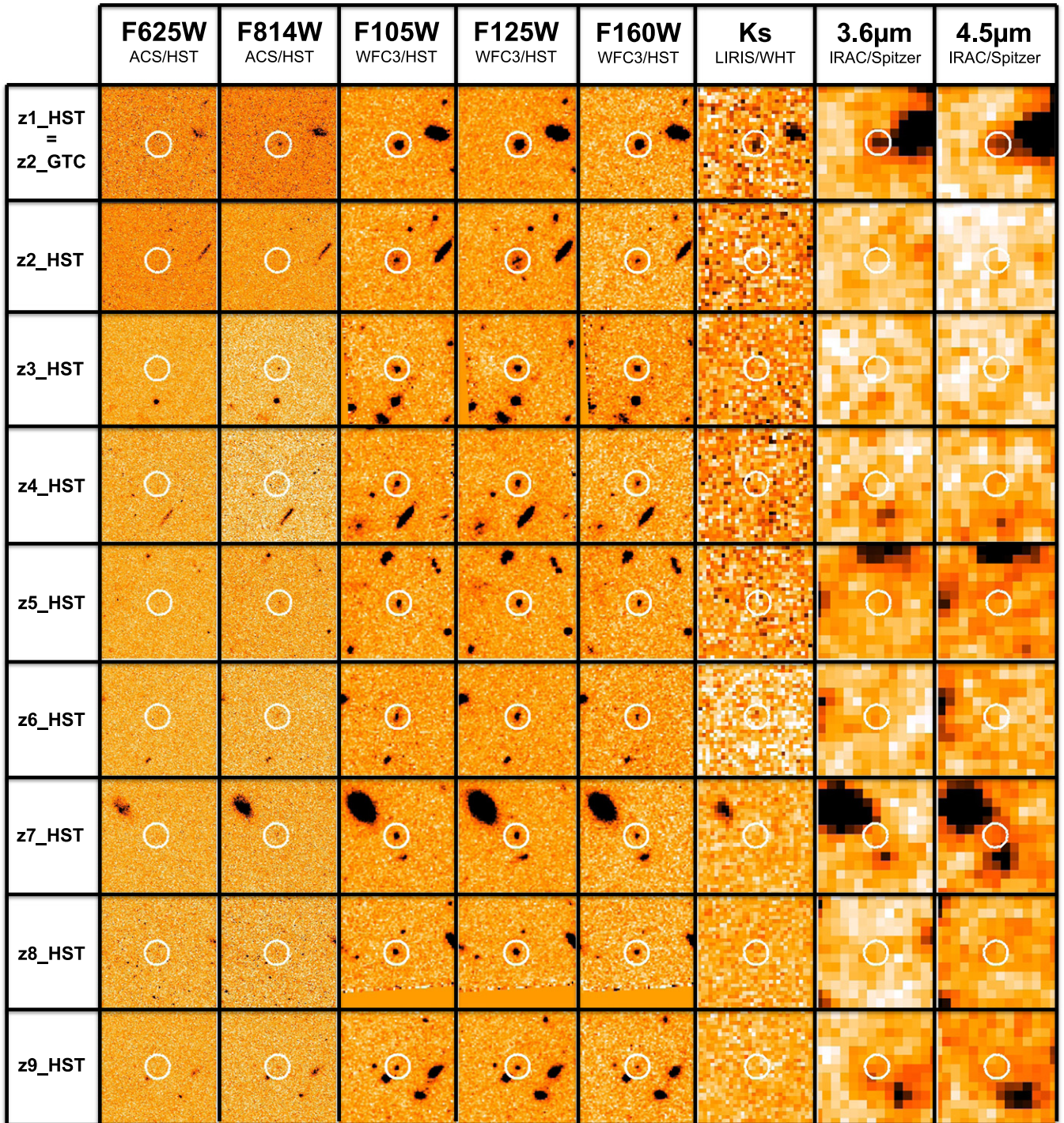


Figure 7. Thumbnail stamp images of the nine candidates selected in the WFC3 field of view. The size of each stamp is $7''.5 \times 7''.5$ in all the bands. The position of the candidate is displayed by a white circle of $0''.8$ radius aperture.

break is not high enough, and even if we used the 1σ detection as an upper limit in F625W, we never reach a break of 2 mag in these two filters (as in previous studies; e.g., Monna et al. 2014). This is why we primarily use here the deeper ground-based GTC g -band data to identify the interlopers.

3.5. Expected Number of Objects

The effective surface covered by our OSIRIS survey is 55.5 arcmin^2 and has been computed by masking all the bright objects on our χ^2 detection picture. We computed the expected

number of sources in that field of view by using the shape of the LF published by Bouwens et al. (2012), which is relatively well established at $z \sim 6$. Including cosmic variance and uncertainties on the Schechter parameters, the expected number of objects in the range of redshift $5.5 < z < 6.5$ and with $m_z < 25.9$ is $1.3^{+2.0}_{-0.9}$, showing that our sample built from GTC data is in excellent agreement with the expectation. For the *HST* survey covering an effective surface of 4.54 arcmin^2 , the expected number of objects detected at more than 5σ with WFC3 bands in the same area is $6.10^{+9.0}_{-4.1}$ (including cosmic

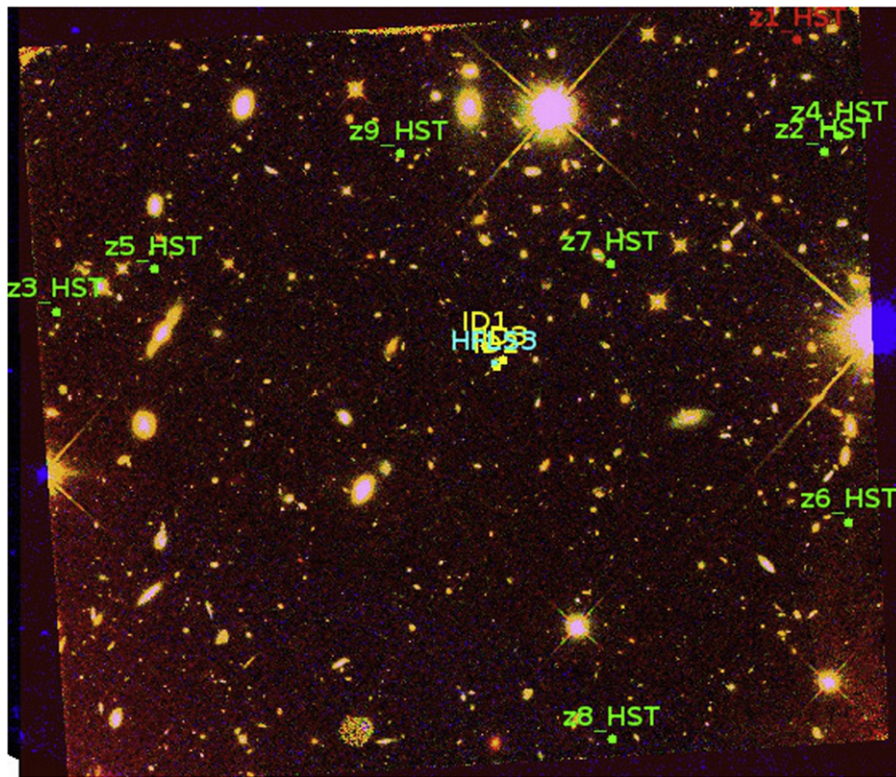


Figure 8. Distribution of our candidates around the submillimeter starburst HFLS3 on a composite image showing the field of view covered by our *HST*/WFC3 data. The position of each candidate is displayed by a green circle (red for the candidate in common in GTC and *HST* samples) and the *Herschel* starburst by a cyan circle. We also plotted the position of the three faint objects discussed in 5.1.

variance). Therefore, our selection is in relatively good agreement with the expectations, without any evidence for a significant overdensity.

4. PHOTOMETRIC PROPERTIES OF THE $z \sim 6$ CANDIDATES

This section presents the principal photometric properties of the selected objects using an SED-fitting approach. We discuss in the following the photometric redshift, UV luminosity, SFR, and reddening for our two samples.

We used version 12.2 of Hyperz³¹ (Bolzonella et al. 2000) with the standard template library, including Bruzual & Charlot (2003), Coleman et al. (1980), Kinney et al. (1996), Polletta et al. (2007), and Silva et al. (1998) templates. The redshift space parameters range from $z \sim 0$ to 8 and A_v from 0.0 to 3.0 mag. The best fit is always found at $z > 5.3$ with a reasonable reddening solution for most of the candidates ($A_v < 1.00$ mag). The redshift probability distribution, hereafter $P(z)$, is well defined around the best photo- z , and no low- z solution appears clearly for all our targets. For the candidate in common in the two samples, we estimated its properties in three cases: (1) combining all of the data points we have; (2) using only the GTC, WHT, and *Spitzer* photometry; and (3) using the *HST*, WHT, and *Spitzer* constraints. The results are similar and give a moderate reddening solution ($A_v \sim 1.80$ – 2.0) and a best photo- z included between 5.8 and 6.1.

As a cross-check, we also tried to fit the SEDs of all these dropouts assuming a low- z solution, i.e., with a redshift space parameter ranging from 0.0 to 3.0 and allowing the same

reddening interval. The best fit is found, in each case, with a higher χ^2 and a $P(z)$ not well defined in the redshift interval explored (see Table 4). We also used a prior in luminosity to check the consistency of our sample with previous studies at $z \sim 6$. The prior was defined using the parameterization of the Schechter function published in Bouwens et al. (2014). The parameter space was defined as previously, and the same template library was used. Two candidates showed different best-fit photo- z 's, but the best-fit SED template was always found at $z > 5.5$.

The UV luminosities were computed using the best-fit SEDs found by Hyperz, and the SFRs were computed from the UV luminosities using the relationship published in Kennicutt (1998). We corrected for the dust extinction of L_{1500} following the Calzetti et al. (2000) method. We noticed that the L_{1500} is ranging from ~ 2.5 to $29 \times 10^{41} \text{erg s}^{-1} \text{\AA}^{-1}$ and the SFRs from ~ 26 to $300 M_{\odot} \text{yr}^{-1}$. These values are in good agreement with expectations for $z > 6$ galaxies (e.g., Schaerer & de Barros 2010) and with properties of previous samples at $z \sim 6$ – 7 (Zheng et al. 2009; Curtis-Lake et al. 2013).

The estimation of the photometric redshift generally implies the use of templates of nearby galaxies extrapolated to the very high z . We made use of the large number of $z \sim 6$ galaxies spectroscopically confirmed to check the reliability of our template library and the SED-fitting method using data from Toshikawa et al. (2012), Jiang et al. (2013), and Willott et al. (2013). We matched photometric catalogs published in previous references to the quality of our data set, more especially for the filters used here in the wavelength range covered by our data (from 0.4 to 1.6 μm). We recomputed photometric error bars of spectroscopically confirmed galaxies using the average noise measured in each of

³¹ <http://userpages.irap.omp.eu/~rpello/newhyperz/>

Table 4
Photometric Properties of the $z \sim 6$ Galaxy Candidates Selected in This Study

ID	High- z				Low- z			Physical Properties	
	z_{phot}	χ^2	A_V (mag)	1σ Interval	z_{phot}	χ^2	A_V (mag)	L_{1500} ($\times 10^{41} \text{erg s}^{-1} \text{\AA}^{-1}$)	SFR [$M_{\odot} \text{yr}^{-1}$]
z1_GTC	6.5	0.6	0.8	6.3–6.5	1.1	2.2	0.0	28.8	302.8
z2_GTC	6.1	0.5	1.8	5.8–6.3	1.5	0.8	0.8	22.5	236.0
z2_HST	6.5	1.5	0.2	6.0–7.2	1.4	4.6	0.0	4.5	47.0
z3_HST	6.2	0.7	0.8	5.7–6.6	1.5	2.0	0.0	16.1	169.3
z4_HST	6.4	0.3	0.8	5.7–7.8	1.5	1.3	0.0	11.6	121.8
z5_HST	7.1	0.07	0.4	5.7–8.0	1.5	1.3	0.0	5.3	56.2
z6_HST	7.1	0.02	0.2	5.8–8.0	1.5	1.3	0.0	3.2	33.2
z7_HST	5.6	0.2	0.8	4.1–6.2	0.1	0.3	0.4	8.2	86.0
z8_HST	6.2	0.3	0.8	5.3–7.4	1.5	0.6	0.0	8.5	89.5
z9_HST	5.2	0.03	0.6	0.0–6.1	0.9	0.1	2.2	2.5	26.2

Note. Information given in this table: (1) ID; (2–5) photo- z , χ_{red} , A_V , and 1σ confidence interval from the best SED fit with a redshift parameter space ranging from $z \sim 0$ to 8; (6–8) photo- z , χ_{red} , and A_V for the best SED fit assuming a low- z solution ($0 < z < 3$); (9, 10) L_{1500} deduced from the best SED fit and SFR computed using the Kennicutt (1998) relation and corrected for dust extinction.

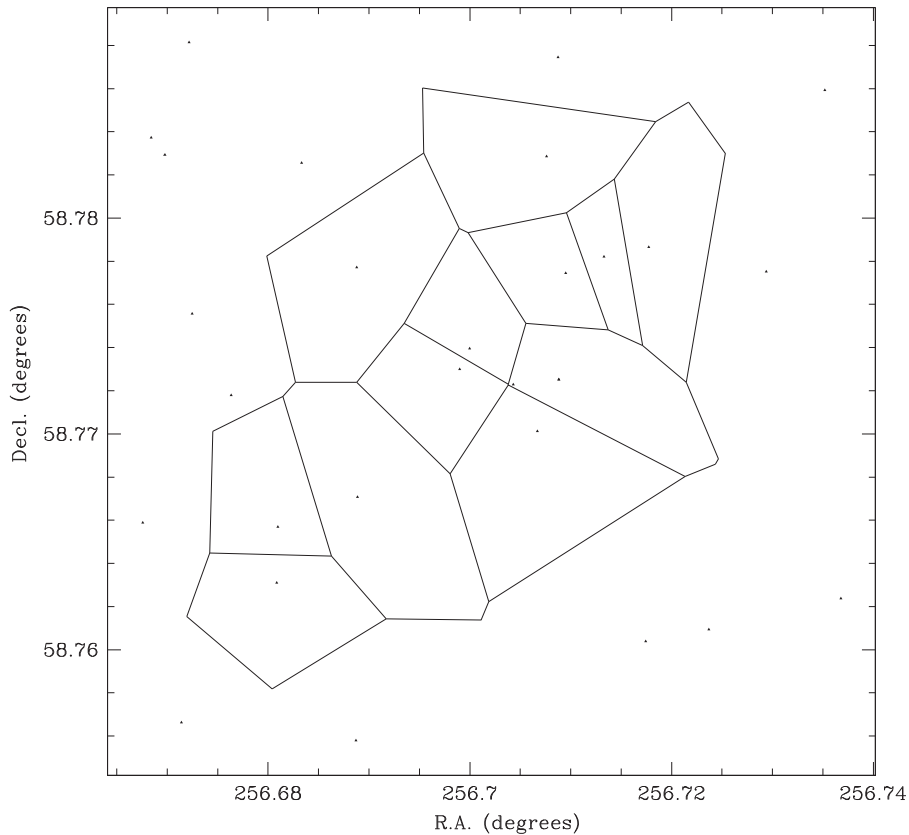


Figure 9. Results of the Voronoi tessellation analysis following the method described in Ramella et al. (2001) on the sample of faint sources described in 5.1. The background threshold above which fluctuations are consistent with an overdense field is estimated at 1.74 per Voronoi cell, which is not a significant detection of an overdensity in the imaging data.

our images. In the case of a nondetection, we used the upper limits computed in our data. The photometric redshift of the confirmed $z \sim 6$ galaxies was computed with Hyperz using the same templates as were used previously with the actual sample. Among the 50 galaxies used, 45 have a 1σ confidence interval for the photometric redshift that includes the spectroscopic redshift. The mean absolute dilation to the spectroscopic redshift is $\sim 9\%$ with a standard deviation of $\sim 16\%$, showing that the method we used to estimate the photometric redshift of our candidates is efficient at $z \sim 6$. We

also used this spectroscopic sample to check the reliability of our color criteria and demonstrated that all these spectroscopically confirmed galaxies would be selected using the criteria defined in Section 3.

5. ENVIRONMENT OF HFLS3

In this section we describe the environment of the starburst galaxy HFLS3 and discuss the possibility of an overdensity associated with it.

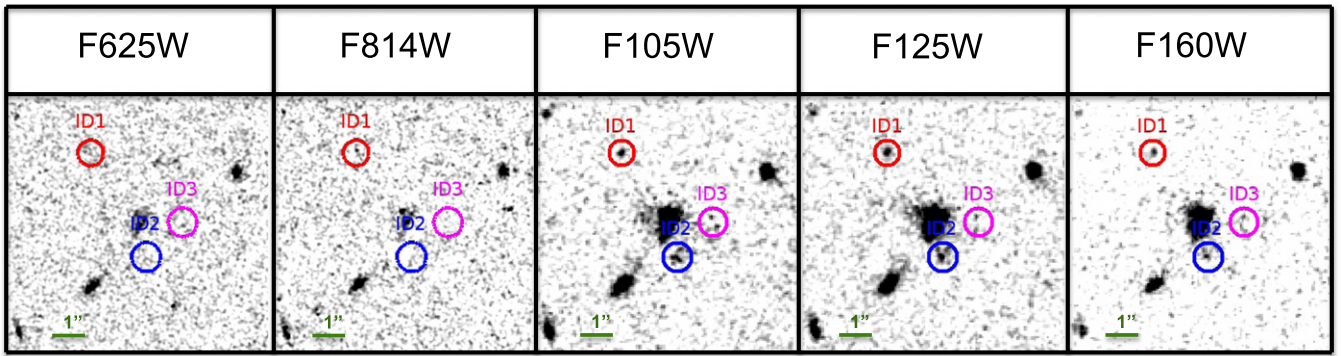


Figure 10. Thumbnail images of the faint sources located around HFLS3. The size of each stamp is $\sim 8''.3 \times 8''.3$. The lens system studied in Cooray et al. (2014) is at the center of the field. The position of each faint candidate is shown by a circle.

5.1. Faint $z \sim 6$ Candidates over the Wide Field

In order to select faintest objects at the redshift of HFLS3, we relaxed the detection constraints we imposed for our *HST* selection Equation (4) by requiring a detection $\geq 3\sigma$ in F105W and F125W (instead of the 5σ level required previously on F105W) and by using the F814W–F105W color criterion computed previously. Indeed, by relaxing the detection level on the F105W image, we are not able to use the color criterion combining F625W and F814W, because of the shallower depth of the F625W. After visual inspection removing false detection as explained above, 25 objects satisfy this new selection function. In order to study whether this sample of faint objects shows any evidence for an overdensity of galaxies associated with HFLS3, we applied the Voronoi tessellation method as described in Ramella et al. (2001) and based on the “triangle” C code. The density threshold we used to distinguish background regions and fluctuations that are significant overdensities is estimated at 1.74 objects per Voronoi cell. As seen in Figure 9, no overdense region is highlighted by the new faint object sample.

However, we noticed that three sources close to HFLS3 (with $26.5 < m_{F105W} < 28.0$) are not detected on ACS data (Figures 10 and 12). Their break between F814W and F105W is < 1 mag, and their NIR colors could be consistent with the Balmer break; therefore, we cannot exclude a low- z solution for these three objects. Assuming that these three sources are at the redshift of HFLS3, the projected distance between them and the *Herschel* starburst is less than 15 kpc. We also compared the overdensity of objects with brightness similar to these three objects over the entire field of view covered by *HST*. The mean density over the field is 0.03 objects per arcsec², whereas it is $4\times$ more around HFLS3, reinforcing the overdensity hypothesis close to the *Herschel* starburst. We applied the same SED-fitting method described above with the same library of templates. We first allowed a large range of redshift ($0 < z < 8$) but found all these objects to be described SEDs compatible with the SED of a $z \sim 6.3$ galaxy. However, we have to keep in mind that the large error bars, as well as the small break between F814W and F105W, could not exclude a low- z solution for all of them. Deep ACS and WFC3 data are needed to strongly increase the nondetection constraints in optical and reduce the error bars on the WFC3 photometry.

5.2. Discussion

In order to constrain the size of a possible overdensity, we adopted the galaxy fluctuation parameter defined in Morselli et al. (2014):

$$\delta = \frac{\rho}{\bar{\rho}} - 1 \quad (9)$$

where ρ is the number of objects selected in our survey and $\bar{\rho}$ the number of objects expected in a blank field covering the same area.

We then compared the number of objects selected in a luminosity range where the completeness is $\sim 100\%$ with the number of objects expected in the same interval in magnitude in a blank field. We computed the completeness level of the F105W image, where the L_{1500} is estimated, by adding 10,000 sources per bin of 0.25 mag. We then applied the extraction parameters explained in Section 2.3 and compared the number of sources extracted with the number of objects added on the image. We showed that $\sim 100\%$ of our added objects are detected up to $m_{F105W} < 25.3$. Three objects in our *HST* sample are brighter than this magnitude cut. We used the UV LF parameterization published in McLure et al. (2009), Su et al. (2011), and Bouwens et al. (2012, 2014) to estimate the number of $z \sim 6$ galaxies expected in our *HST* survey with $m_{F105W} < 25.3$ (see Table 6). The expected number of objects ranges from 0.5 to 1.0; therefore, the overdensity parameter ranges from 2.4 to 9.15, with 9.15 as a strict upper limit on the overdensity given the cosmic variance and taking into account the contamination rate computed in Section 3.4. We emphasize that this result is based on a small field of view and a small number of objects. Chapman (2009) found a similar value ($\delta \sim 2.5$) for UV-selected galaxies over the GOODS-N field and noticed that this value is lower than that found for sub-millimeter galaxies (SMGs) in the same field ($\delta \sim 10$). As shown by Robson et al. (2014), there is no overdensity of SMGs around HFLS3. If an overdensity occurs around HFLS3, it is at a lower level than in the COSMOS AzTEC-3 field (Capak et al. 2011), where they found an overdensity factor of 11.

We note that four galaxies among our two samples have high SFRs estimated from the SED models (with SFRs $> 100 M_{\odot} \text{ yr}^{-1}$). These sources, however, are undetected in the SCUBA-2 850 μm image of this field (Robson et al. 2014), with a noise level of $\sim 1.5 \text{ mJy beam}^{-1}$. Riechers et al. (2014) have studied with ALMA the center of the galaxy protocluster associated

Table 5
UV LF Parameterization at $z \sim 6$

Reference	M^*	Φ^* $\times 10^{-3}(\text{Mpc}^{-3} \text{mag}^{-1})$	α
This work	$-20.16^{+0.35}_{-0.15}$	$1.36^{+0.40}_{-0.19}$	-1.70 ± 0.23
McLure et al. (2009)	-20.04 ± 0.12	1.80 ± 0.50	-1.71 ± 0.11
Su et al. (2011)	-20.25 ± 0.23	$1.77^{+0.62}_{-0.49}$	-1.87 ± 0.14
Bouwens et al. (2012)	-20.37 ± 0.30	$1.4^{+1.1}_{-0.6}$	-1.73 ± 0.22
Bouwens et al. (2014)	-20.93 ± 0.25	$0.49^{+0.26}_{-0.17}$	-1.85 ± 0.10

Note. Parameterization of the Schechter function presented in this paper and published by other teams.

Table 6
Number Density at $z \sim 6$

M_{1500}	$\Phi(M_{1500})$ $\times 10^{-4}(\text{Mpc}^{-3} \text{mag}^{-1})$	$d\Phi$ $\times 10^{-4}(\text{Mpc}^{-3} \text{mag}^{-1})$
-21.75 ± 0.250	0.09	$^{+0.23}_{-0.09}$
-21.25 ± 0.250	1.01	± 0.49
-20.75 ± 0.500	2.60	± 1.22

Note. Number density computed following a method using the redshift probability distribution. Error bars included Poisson uncertainties and cosmic variance computed from Trenti & Stavielli (2008).

with the $z = 5.3$ SMG AzTEC-3 (Capak et al. 2011), but they failed to detect an LBG at $z = 5.3$ with an SFR $\sim 20 M_{\odot} \text{yr}^{-1}$ with ALMA data reaching $\sim 0.15 \text{ mJy beam}^{-1}$ (3σ) at 1 mm. Assuming a typical T_{dust} of 35 K for the HFLS3 LBGs, a colder dust temperature than HFLS3, observed-frame $850 \mu\text{m}$ lies on the Wien part of the SED and the K -correction from $z = 5.3$ to $z = 6.3$ remains positive. Scaling the SED and depths reached between ALMA at $z = 5.3$ at 1 mm and SCUBA-2 for galaxies at $z \sim 6.3$ at $850 \mu\text{m}$, we find that the SCUBA-2 depth is only adequate to detect galaxies above 3σ with instantaneous SFRs $> 500 M_{\odot} \text{yr}^{-1}$. This ignores the cosmic microwave background (CMB) that will absorb a few percent of the submillimeter flux at $z = 6.3$ compared to $z = 5.3$. Therefore, SCUBA-2 observations of the depth of the Robson et al. (2014) data are unlikely to detect galaxies with similar SFRs and SED properties to LBGs in the AzTEC-3 protocluster.

5.3. Distribution in Luminosity of the $z \sim 6$ Candidates

The redshift interval covered by our survey is sufficient to compute the UV LF at $z \sim 6$. This again allows a way to study whether there is an overdensity of objects at a given luminosity. Several methods have been developed to compute the UV LF at different redshifts (e.g., Bouwens 2012; Willott et al. 2013). We made use of the previous SED-fitting work to compute the number density of objects at $z \sim 6$ as a function of the UV luminosity (see Laporte et al. 2015 for details).

The effective surface explored by our *HST* survey is computed by masking the bright objects on the detection image. The comoving volume explored between $z \sim 5.5$ and $z \sim 6.5$ is $V \approx 10,980 \text{ Mpc}^3$. The number densities we found are shown in Table 5, and the error bars take into account the cosmic variance. These numbers are consistent with previous

findings in this redshift interval (e.g., Bouwens et al. 2007; Willott et al. 2013).

We adopted the Schechter parameterization (Schechter 1976) of the UV LF, defined by

$$\Phi(M) = \Phi^* \frac{\ln(10)}{2.5} \left(10^{-0.4(M-M^*)}\right)^{\alpha+1} \exp\left(-10^{-0.4(M-M^*)}\right) \quad (10)$$

where M^* , Φ^* , and α are the three Schechter parameters to be adjusted.

In order to show the influence of the densities computed in this study, we fitted the shape of the UV LF by combining them with the density from Bouwens et al. (2014) in the faint-end slope and in the bright end with those published by Willott et al. (2013). We used a χ^2 minimization with parameters ranging from 10^{-5} to $10^{-2} \text{ Mpc}^{-3} \text{mag}^{-1}$, -22.0 to -19.0 , and -2.2 to -1.1 , respectively, for Φ^* , M^* , and α . The following parameterization is found at $z \sim 6$: $M^* = -20.17^{+0.35}_{-0.15}$, $\Phi^* = (1.21^{+0.40}_{-0.19}) \times 10^{-3} \text{ Mpc}^{-3} \text{mag}^{-1}$, and $\alpha = -1.77 \pm 0.23$. Error bars on each parameter are deduced from the 1σ confidence interval. These parameters are in good agreement with previous results (e.g., McLure et al. 2009; Su et al. 2011; Bouwens et al. 2012; Table 6). The shape of the UV LF deduced from this study and the number densities we computed are plotted in Figure 11. We find no evidence for an overdensity of galaxies, above the field LF, at any of the luminosities probed by the data.

6. CONCLUSIONS

We have presented in this paper the results of the photometric analysis of the environment of a submillimeter starburst at $z \sim 6.34$, combining both wide-area ground-based data and high-level quality *HST* data to explore a large range of luminosities. We applied the LBG selection technique and found 10 galaxies that are at $z \sim 6$. This sample includes two from our ground-based search ($m_z \sim 25$) and eight more from our search with *HST*/WFC3 data (with m_{F105W} in the range 24.5–26.5). The size of each sample is well consistent with expectations from previous findings using blank-field surveys and seems incompatible with an overdensity of luminous ($m_{\text{F105}} < 25.9$) galaxies. We used a standard method to estimate the photometric properties of each source, and we used these SED-fitting results to compute the UV LF at $z \sim 6$. The parameterization of the Schechter function we deduced ($M^* = -20.17^{+0.35}_{-0.15}$, $\Phi^* = (1.21^{+0.40}_{-0.19}) \times 10^{-3} \text{ Mpc}^{-3}$ and

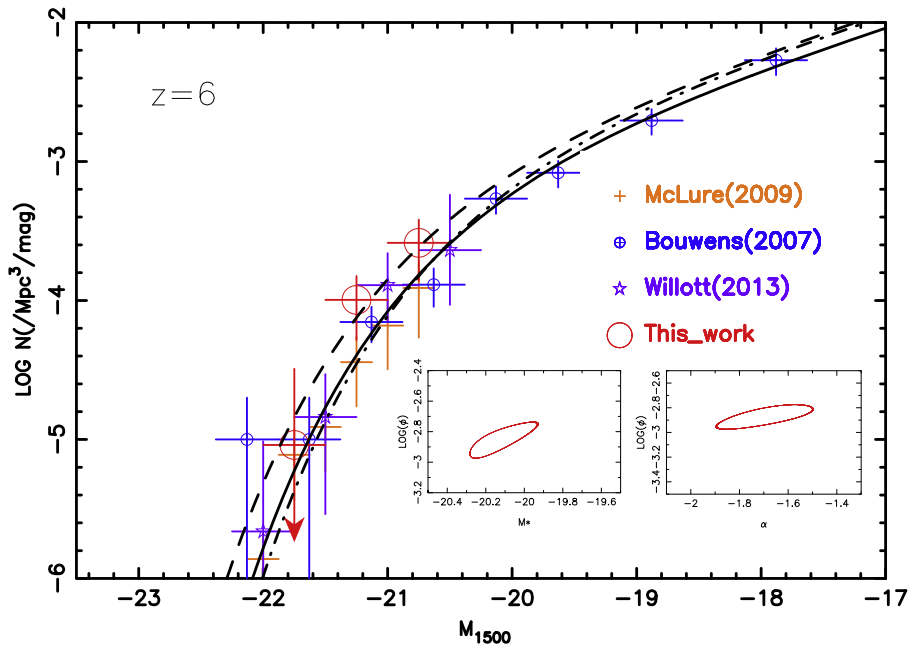


Figure 11. Shape of the UV LF at $z \sim 6$. Number densities from this study are plotted in red; previous findings are also plotted (Bouwens et al. 2007; McLure et al. 2009; Willott et al. 2013). The parameterization computed from the study of the HFLS3 environment is displayed by the black line; the other lines display the parameterization published in previous references (dashed line from Bouwens et al. 2012; dot-dashed line from McLure et al. 2009). The 1σ confidence intervals on each parameter are also shown in the lower panels.

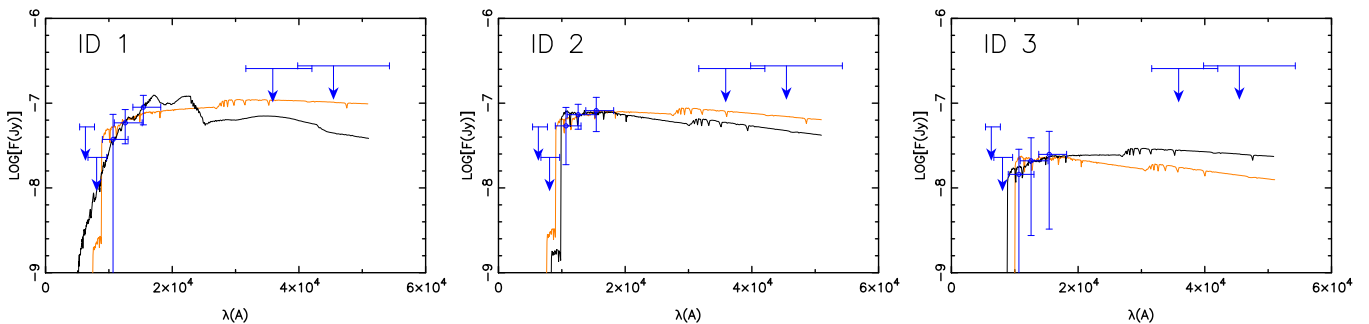


Figure 12. SED fitting of the three faint objects highlighted around HFLS3 using two assumptions on the redshift: allowing a large range of redshift $0 < z < 8$ ($\chi^2_{\text{red}} \sim 0.05, 0.02, \text{ and } 0.01$ for ID1, ID2, and ID3, respectively; black line) and fixing the redshift at the redshift of HFLS3 ($\chi^2_{\text{red}} \sim 0.15, 0.06, \text{ and } 0.01$ for ID1, ID2, and ID3, respectively; orange line). The blue dots show the photometry of these three faint objects (SExtractor MAG_AUTO) and the 2σ upper limits in case of nondetection. Error bars are computed using the noise measured in empty apertures around the objects.

$\alpha = -1.77 \pm 0.23$) is in good agreement with previous findings in this redshift interval.

We do not find any strong evidence for HFLS3 being a member of a protocluster of luminous galaxies, as is the case of the well-known SMG Aztec-3 (Capak et al. 2011). There the overdensity parameter was found to be about 11; in the case of HFLS3, we place an upper limit on the overdensity of ≈ 9 after taking into account the cosmic variance of existing $z \sim 6$ LF measurements. The lack of a significant overdensity is also confirmed by a Voronoi tessellation analysis that included all the faint objects fulfilling the color criteria defined for $z \sim 6$ objects, but without a well-defined break between the optical ACS and NIR WFC3 imaging data.

However, we noticed at least three faint objects within $3''$ from HFLS3. They are undetected in ACS images and are detected on WFC3 data. If the redshift of these sources is confirmed at $z \sim 6$, then the *Herschel* starburst is located in an overdense region composed of faint objects but with an extent of 36 kpc. Deeper data combined with spectroscopic

observations are needed to assess these conclusions. It is more likely that these are associations with the merger system that might be triggering the starburst.

Financial support for this work was provided by the Spanish MINECO under projects AYA2010-21697-C05-04 and FIS2012-39162-C06-02, by the Chilean Basal-CATA PFB-06/2007 and CONICYT-Chile under the grant Gemini-CONICYT #32120003, and by NASA through grant HST-GO-13045 from the Space Telescope Science Institute, which is operated by Associated Universities for Research in Astronomy, Inc., under NASA contract NAS 5-26555. Additional support for A.C., W.O., J.C., J. L.W., and C.M.C. was from NSF with AST-1313319. The Dark Cosmology Centre is funded by the Danish National Research Foundation (J.L.W.). S.O. acknowledges support from the Science and Technology Facilities Council [grant number ST/I000976/1]. D.R. acknowledges support from the Science and Technology Facilities Council (ST/K00106X/1). R.J.I. acknowledges support from the European Research Council in the form of Advanced

Grant, COSMICISM, 321302. SPIRE has been developed by a consortium of institutes led by Cardiff Univ. (UK) and including Univ. Lethbridge (Canada); NAOC (China); CEA, LAM (France); IFSI, Univ. Padua (Italy); Stockholm Observatory (Sweden); Imperial College London, RAL, UCL-MSSL, UKATC, Univ. Sussex (UK); and Caltech, JPL, NHSC, Univ. Colorado (USA). This development has been supported by national funding agencies: CSA (Canada); NAOC (China); CEA, CNES, CNRS (France); ASI (Italy); MCINN (Spain); SNSB (Sweden); STFC, UKSA (UK); and NASA (USA). We thank José Acosta-Pulido for advice on the LIRIS observations and help with the LIRIS data reduction package. This work is based on observations made with the Gran Telescopio Canarias (GTC), installed in the Spanish Observatorio del Roque de los Muchachos of the Instituto de Astrofísica de Canarias, on the island of La Palma. The William Herschel Telescope is operated on the island of La Palma by the Isaac Newton Group in the Spanish Observatorio del Roque de los Muchachos of the Instituto de Astrofísica de Canarias. The data presented in this paper will be released through the Herschel Database in Marseille HeDaM (hedam.oamp.fr/HerMES)

Facilities: GTC (OSIRIS), *HST* (ACS, WFC3), *Spitzer* (IRAC), WHT (LIRIS).

REFERENCES

- Ahn, C., Alexandroff, R., Allende, P., et al. *MNRAS*, **427**, 3435
- Alvarez, P., Rodriguez Espinosa, J. M., & Sanchez, F. 1998, *NewAR*, **42**, 553
- Baugh, C. M., Lacey, C. G., Frenk, C. S., et al. 2005, *MNRAS*, **356**, 1191
- Bertin, E. 2006, in ASP Conf. Ser. 351, *Astronomical Data Analysis Software and Systems XV*, ed. C. Gabriel et al. (San Francisco, CA: ASP), **112**
- Bertin, E. 2010, *ascl*, **10068B**
- Bertin, E. 2011, in ASP Conf. Ser. 442, *Astronomical Data Analysis Software and Systems XX (ADASSXX)*, ed. I. N. Evans et al. (San Francisco, CA: ASP), **435**
- Bertin, E., & Arnouts, S. 1996, *A&A*, **117**, 393
- Boone, F., Schaerer, D., Pello, R., et al. 2011, *A&A*, **534A**, 124B
- Bouwens, R., Bradley, L., Zitrin, A., et al. 2014, *ApJ*, **795**, 126
- Bouwens, R., Illingworth, G. D., Franx, M., & Ford, H. 2007, *ApJ*, **670**, 928
- Bouwens, R., Illingworth, G. D., Oesch, P., et al. 2012, *ApJ*, **752**, 5
- Bouwens, R., Illingworth, G. D., Oesch, P., et al. 2014, *ApJ*, submitted (arXiv:1403.4295B)
- Bouwens, R., Illingworth, G. D., Oesch, P., et al. 2015, *ApJ*, **803**, 34
- Bolzoni, M., Miralles, J. M., & Pello, R. 2000, *A&A*, **363**, 476
- Bradley, L., Zitrin, A., Coe, D., et al. 2014, *ApJ*, **792**, 76
- Bruzual, G., & Charlot, S. 2003, *MNRAS*, **344**, 1000
- Burgasser, A. 2007, *ApJ*, **658**, 617
- Burgasser, A., Burrows, A., & Kirkpatrick, J. 2006b, *ApJ*, **639**, 1095
- Burgasser, A., Geballe, T. R., Leggett, S. K., Kirkpatrick, J. D., & Golimowski, D. A. 2006c, *ApJ*, **637**, 1067
- Burgasser, A., Liu, M. C., Ireland, M. J., Cruz, K. L., & Dupuy, T. J. 2008, *ApJ*, **681**, 579
- Burgasser, A., & McElwain, M. W. 2006d, *AJ*, **131**, 1007
- Burgasser, A., McElwain, M., Kirkpatrick, J., et al. 2004, *AJ*, **127**, 2856
- Calzetti, D., Armus, L., Bohlin, R. C., et al. 2000, *ApJ*, **533**, 682
- Capak, P., Riechers, D., Scoville, N. Z., et al. 2011, *Natur*, **434**, 738
- Carilli, C. L., Daddi, E., Riechers, D., et al. 2010, *ApJ*, **714**, 1407
- Casey, C. M., Narayanan, D., & Cooray, A. 2014, *PhR*, **541**, 45
- Castellano, M., Fontana, A., Paris, D., et al. 2010, *A&A*, **524**, 28
- Cepa, J., Aguiar-Gonzalez, M., Bland-Hawthorn, J., et al. 2003, *SPIE*, **4841**, 1739
- Chapman, S. C., Blain, A., Ibat, R., et al. 2009, *ApJ*, **691**, 560
- Chiu, K., Fan, X., Leggett, S. K., et al. 2006, *AJ*, **131**, 2722
- Coleman, G. D., Wu, C. C., & Weedman, D. W. 1980, *ApJ*, **43**, 393
- Cooray, A., Calanog, J., Wardlow, J., et al. 2014, *ApJ*, **790**, 40
- Cruz, K. L., Burgasser, A. J., Reid, I. N., & Liebert, J. 2004, *ApJL*, **604**, 61
- Curtis-Lake, E., McLure, R. J., Dunlop, J. S., et al. 2013, *MNRAS*, **429**, 302
- Daddi, E., Dannerbauer, H., Stern, D., et al. 2009, *ApJ*, **694**, 1517
- de Barros, S., Schaerer, D., & Stark, D. 2014, *A&A*, **563A**, 81
- Dowell, C. D., Conley, A., Glenn, J., et al. 2014, *ApJ*, **780**, 75
- Fazio, G. G., Hora, J., Allen, L. E., et al. 2004, *ApJ*, **154**, 10
- Finkelstein, S. L., Papovich, C., Dickinson, M., et al. 2013, *Natur*, **502**, 524
- Finkelstein, S. L., Ryan, R., Papovich, C., et al. 2014, *ApJ*, arXiv:1410.5439
- Fruchter, A. S., & Hook, R. N. 2002, *PASP*, **114**, 144
- Gilmozzi, R., & Spyromilio, J. 2007, *Msngr*, **127**, 11
- Griffin, M., Abergel, A., Abreu, A., et al. 2010, *A&A*, **518**, 3
- Gwyn, S. 2012, *AJ*, **143**, 38
- Hayes, M., Laporte, N., Pello, R., Schaerer, D., & Le Borgne, J. F. 2012, *MNRAS*, **425**, 19
- Hayward, C., Narayanan, D., Keres, D., et al. 2013, *MNRAS*, **428**, 2529
- Hughes, D. H., Serjeant, S., Dunlop, J., et al. 1998, *Natur*, **394**, 241
- Jiang, L., Egami, E., Mechtley, M., et al. 2013, *ApJ*, **772**, 99
- Kennicutt, R. 1998, *A&A*, **36**, 189
- Kinney, A. L., Calzetti, D., Bohlin, R. C., et al. 1996, *ApJ*, **467**, 38
- Kirkpatrick, J. D., Looper, D. L., Burgasser, A. J., et al. 2010, *ApJS*, **190**, 100
- Lacey, C. G., Baugh, C. M., Frenk, C. S., & Benson, A. J. 2011, *MNRAS*, **412**, 1828
- Laporte, N., Streblyanska, A., Clement, B., et al. 2014, *A&A*, **562**, 8
- Laporte, N., Streblyanska, A., Kim, S., et al. 2015, *A&A*, **575A**, 92
- LeFevre, O., Tasca, L. A. M., Cassata, P., et al. 2015, *A&A*, **576A**, 79
- Liebert, J., & Burgasser, A. J. 2007, *AJ*, **655**, 522
- Looper, D. L., Burgasser, A. J., Kirkpatrick, J. D., & Swift, B. J. 2007, *AJ*, **134**, 1162
- Manchado, A., Fuentes, F. J., Prada, F., et al. 1998, *SPIE*, **3354**, 448
- Mauduit, J.-C., Lacy, M., Farrah, D., et al. 2012, *PASP*, **124**, 714
- McElwain, M. W., & Burgasser, A. J. 2006, *AJ*, **132**, 2074
- McLure, R. J., Cirasuolo, M., Dunlop, J. S., Foucaud, S., & Almaini, O. 2009, *MNRAS*, **395**, 2196
- Monna, A., Seitz, S., Greisel, N., et al. 2014, *MNRAS*, **438**, 1417
- Morselli, L., Mignoli, M., Gilli, R., et al. 2014, *A&A*, **568A**, 1
- Muzzin, A., Marchesini, D., Stefanon, M., et al. 2013, *ApJ*, **206**, 8
- Oesch, P., Bouwens, R., Carollo, C. M., et al. 2010, *ApJL*, **709**, L21
- Oke, J. B., & Gunn, J. E. *ApJ*, **266**, 713
- Oliver, S., Bock, J., Altieri, B., et al. 2012, *MNRAS*, **424**, 1614
- Pilbratt, G. L., Riedinger, J. R., Passvogel, T., et al. 2010, *A&A*, **518**, 1
- Pirard, J.-F., Kissler-Patig, M., Moorwood, A., et al. 2004, *SPIE*, **5492**, 1763
- Polletta, M., Tajer, M., Maraschi, L., et al. 2007, *ApJ*, **663**, 81
- Ramella, M., Boschin, W., Fadda, D., & Nonino, M. 2001, *A&A*, **368**, 776
- Reid, I. N., Lewitus, E., Burgasser, A. J., & Cruz, K. L. 2006, *ApJ*, **639**, 1114
- Richard, J., Pello, R., Schaerer, D., LeBorgne, J. F., & Kneib, J. P. 2006, *A&A*, **456**, 861
- Riechers, D., Bradford, C. M., Clements, D. L., et al. 2013, *Natur*, **496**, 329
- Riechers, D., Carilli, C. L., Capak, P., et al. 2014, *ApJ*, **796**, 84
- Robberto, M., Baggett, S. M., Hilbert, B., et al. 2004, *SPIE*, **5499**, 15
- Robson, E. I., Ivison, R. J., Smail, I., et al. 2014, *ApJ*, **793**, 11
- Schaerer, D., & de Barros, S. 2010, *A&A*, **515**, 73
- Schechter, P. 1976, *ApJ*, **203**, 297
- Schenker, M. A., Stark, D., Ellis, R. S., et al. 2012, *ApJ*, **744**, 179
- Scoville, N., Abraham, R. G., Aussel, H., et al. 2007, *ApJ*, **172**, 38
- Sheppard, S. S., & Cushing, M. C. 2009, *AJ*, **137**, 304
- Siegler, N., Close, L. M., Burgasser, A. J., et al. 2007, *AJ*, **133**, 2320
- Silva, L., Granato, G. L., Bressan, A., & Danese, L. 1998, *ApJ*, **509**, 103
- Smail, I., Ivison, R. J., & Blain, A. W. 1997, *ApJL*, **490**, L5
- Steidel, C., Giavalisco, M., Pettini, M., Dickinson, M., & Adelberger, K. L. 1996, *ApJ*, **462**, 17
- Su, J., Stiavelli, M., Oesch, P., et al. 2011, *ApJ*, **738**, 123
- Szalay, A., Connolly, A. J., & Szokoly, G. P. 1999, *AJ*, **117**, 685
- Taylor, M. B. 2005, in ASP Conf. Ser. 347, *Astronomical Data Analysis Software and Systems XIV*, ed. P. L. Shopbell, M. C. Britton, & R. Ebert (San Francisco, CA: ASP), **29**
- Toshikawa, J., Kashikawa, N., Ota, K., et al. 2012, *ApJ*, **750**, 137
- Trenti, M., Bradley, L. D., Stiavelli, M., et al. 2012, *ApJ*, **746**, 55
- Trenti, M., & Stiavelli, M. 2008, *ApJ*, **676**, 767
- Vanzella, E., Pentericci, L., & Fontana, A. 2011, *ApJL*, **730**, L35
- Wall, J. V. 1987, *JBAA*, **98**, 8
- Willott, C., McLure, R. J., Hibon, P., et al. 2013, *AJ*, **145**, 4
- Zheng, W., Bradley, L. D., Bouwens, R., et al. 2009, *ApJ*, **697**, 1907